

● *Original Contribution*

## IMPROVED METHOD FOR DETERMINING RESOLUTION ZONES IN ULTRASOUND PHANTOMS WITH SPHERICAL SIMULATED LESIONS

JAMES M. KOFLER, JR.\* and ERNEST L. MADSEN†

\*Department of Radiology, Mayo Clinic, Rochester, MN, USA; and †Department of Medical Physics, University of Wisconsin, Madison, WI, USA

(Received 7 March 2001; in final form 17 September 2001)

**Abstract**—Quantification of ultrasound (US) imager performance simulating human observers is addressed using size-dependent lesion signal-to-noise ratio (*LSNR*) analysis of images of spherical simulated lesions in phantoms. *LSNR* values obtained over a broad range of image depths can be used with a single detectability threshold to determine the depth range over which lesions of a given size and contrast are deemed to be detectable, yielding a performance metric. Optimal *LSNR* analysis requires *a priori* knowledge of lesion locations in the image so that *LSNR* values relate to the center of each lesion. Phantoms having a regular array of accurately positioned spherical simulated lesions are described, along with easily employed and robust software that accurately determines lesion locations in images, even when only a few are detectable by visual inspection. The software accounts for image spatial calibration inaccuracies and accommodates sector, curvilinear, *etc.*, formats. The minimum number of equivalent lesions to yield an acceptable mean (counteracting speckle variations) also is addressed. (E-mail: jkofler@mayo.edu) © 2002 World Federation for Ultrasound in Medicine & Biology.

**Key Words:** Automation, Detectability, Performance, Quality assurance, Resolution, Phantom, Spherical lesions.

### INTRODUCTION

One of the challenges for any imaging modality is to provide for the detection of small low-contrast objects in the image. Generally, there are spatially random variations in image grey levels, referred to as noise, that reduce the likelihood of detection. Determination of detectability of small well-characterized low-contrast lesions is important for quantifying the image performance of a system.

If the imaging system is tomographic (*i.e.*, presents an image of a “slice” of the patient), then the imaging process involves three dimensions (3-D): two dimensions parallel to the slice and one perpendicular to it. Considering the dimension perpendicular to the slice, a small sphere with diameter much less than the “slice width” may not be detectable, whereas a cylinder of the same composition and diameter, aligned perpendicularly to the slice, could be easily detected (Madsen et al. 1991). The difference in detectability is due to the partial volume effect. Spherical low-contrast objects (targets)

are preferred for testing tomographic imagers because they have no preferred alignment, as is the case for most objects imaged in the human body.

Ultrasonically, tissue-mimicking phantoms with a spatially random distribution of equal-diameter and equal-object-contrast<sup>1</sup> spheres have been reported (Madsen et al. 1991) for testing the performance of US scanners where human observers determined depth ranges over which spheres of given diameter and contrast were detectable; such a depth range is referred to as a resolution zone.

*The “matched filter” method for computing detectability*

Direct human observer determination of such detectability depth ranges (resolution zones), can be too

<sup>1</sup>Object contrast is defined as:

$$10 \log_{10} \left[ \frac{BSC_{obj}}{BSC_{ref}} \right],$$

where  $BSC_{obj}$  and  $BSC_{ref}$  are the backscatter coefficients of the object and reference material, respectively. The reference or background material usually surrounds the object. Image contrast refers to the contrast of the object as rendered on the display and considers the assignment of echo amplitude signals to grey-scale values.

Address correspondence to: James M. Kofler, Jr., Department of Diagnostic Radiology, Mayo Clinic, Rochester, MN 55905 USA. E-mail: jkofler@mayo.edu

time-consuming to be practical. A method for computing the likelihood of detection of a target has been described previously (Wagner and Brown 1985; Lopez et al. 1992; Rownd et al. 1997). The method is referred to as the “matched filter” method and can be considered as an attempt to simulate detection by a human observer. The detectability of a specific lesion is defined in the form of a lesion signal-to-noise ratio,  $LSNR$ , viz.:

$$LSNR \equiv \frac{S_L - S_B}{[(1/2)(\sigma_B^2 + \sigma_L^2)]^{1/2}}, \quad (1)$$

where  $S_L$  is the average pixel value over the area corresponding to the lesion,  $S_B$  is the mean pixel value over an equal area of “background” surrounding the lesion,  $\sigma_B^2$  is the variance of a sufficiently large number of independent realizations of  $S_B$ , and  $\sigma_L^2$  is the variance of a sufficiently large number of independent realizations of  $S_L$ . (“Independent realizations” are values that are computed from equivalent regions of the image that do not overlap and, therefore, do not share noise components.) Image noise, however, will result in the  $LSNR$  for two different lesions at the same depth being different, even though the two lesions have the same diameter and object contrast. Thus, the most useful form of  $LSNR$  is that in which means over many values of  $S_L$  and  $S_B$  are represented in the numerator. We define

$$LSNR_M \equiv \frac{S_{ML} - S_{MB}}{[(1/2)(\sigma_B^2 + \sigma_L^2)]^{1/2}}, \quad (2)$$

where  $S_{ML} \equiv (1/N)\sum_{i=1}^N S_{Li}$ ,  $S_{Li}$  being the average pixel value over the area of the  $i$ th independent realization of a target. In like manner,  $S_{MB} \equiv (1/N)\sum_{i=1}^N S_{Bi}$ . The  $N$  values of  $S_{Li}$  and of  $S_{Bi}$  can be used in the computation of  $\sigma_B^2$  and  $\sigma_L^2$ .

As in the two previous cases employing  $LSNR$  ratios to assess detectability (Lopez et al. 1992; Rownd et al. 1997), the approximation is made that  $\sigma_B^2 \approx \sigma_L^2$ . The latter relation applies particularly when the lesions are barely detectable. Thus, we have:

$$LSNR \approx \frac{S_L - S_B}{\sigma_B} \quad (3)$$

$$LSNR_M \approx \frac{S_{ML} - S_{MB}}{\sigma_B} \quad (4)$$

#### *Ad hoc matched filter method*

A method has been reported (Rownd et al. 1997) for employing  $LSNR$  computations to determine depth ranges where detection occurs for spherical simulated lesions with

given diameter and object contrast. A set of tissue-mimicking phantoms were employed, each having a coplanar, approximately regular, array of spherical lesions of the same diameter and contrast, extending from the scanning window to a depth of about 16 cm. Unfortunately, although the centers of the spheres were precisely coplanar, the manufacturing process did not assure precise placement of the spheres in the array; the uncertainty in position of any sphere was as much as 3 mm. This uncertainty precluded exact determinations of sphere positions in images of the phantom; therefore, computation of  $LSNR$  or  $LSNR_M$  values could not be accomplished.

#### *System allowing computation of $LSNR_M$ values with known lesion positions in the image*

In the present report, a system is described for determining detection depth ranges for spherical simulated lesions using phantoms with arrays of precisely positioned lesions. The exact relative positioning of the spheres in the array allows software determination of the positions of all target spheres in the image, which then allows computation of  $LSNR_M$  values for target lesions. Thus, a single threshold value on  $LSNR_M$  is needed.

## MATERIALS AND METHODS

### *Phantom production*

The technique for embedding simulated lesions at precise locations within a tissue-mimicking (TM) background material incorporates a machined template that contains projecting spherical segments placed in a perfect array. (The template is made using a ball end mill to create a regular array of depressions in a planar acrylic plate. The depressions have a radius of curvature equal to the radius  $r$  of the intended lesions, and the depth of the depressions equals  $r/2$ . Acrylic spheres of radius  $r$  are glued into the depressions, creating spherical segments projecting  $1.5 r$  above the planar surface.) The template is affixed as a single side of a phantom “half” mold. Molten TM background material is then poured into the mold and allowed to congeal. The apparatus is continuously rotated during congealing of the gel to prevent sedimentation. The template is then removed, leaving an exact array of spherical segment depressions on the surface of the solidified TM material. A spherical simulated lesion is then pressed into each depression, and the second half of the phantom is filled with background TM material. The “lips” of the depressions hold the agar spheres in position. Figures 1 and 2 show a schematic and a US image of a spherical lesion phantom with exactly positioned spheres. Distances between spheres are estimated to be within 0.2 mm of the expected perfect array distances. Several types of spherical lesion phantoms exist, including phantoms with sphere diameters of 2,

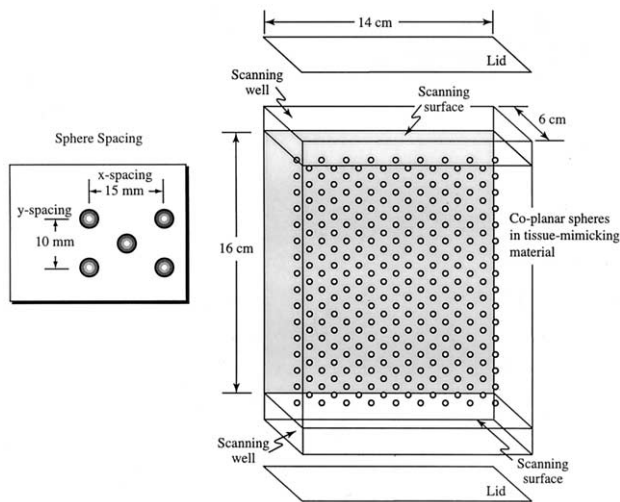
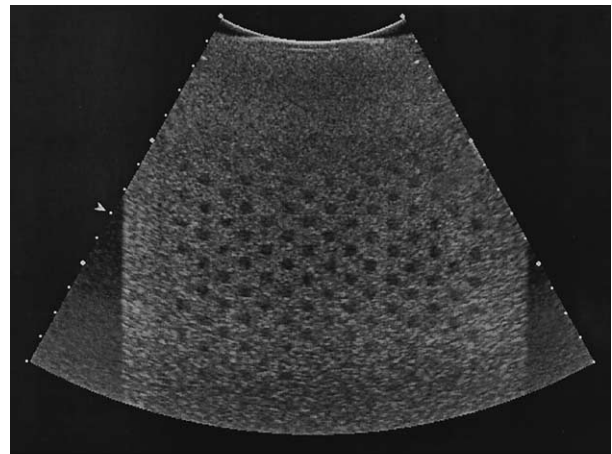


Fig. 1. A schematic of a spherical lesion phantom. Note that each phantom contains simulated lesions that are identical in size and object contrast.

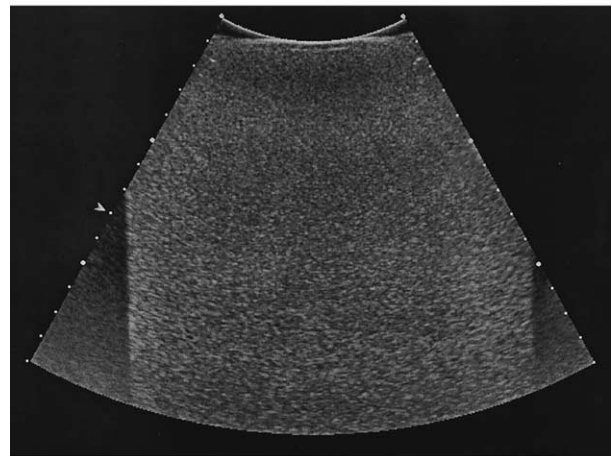
3, 4, 5 and 6 mm and with object contrasts of  $-3$  dB,  $-6$  dB,  $-9$  dB,  $-14$  dB, and  $+3$  dB.

*Image acquisition*

Careful alignment of the plane of symmetry of the scan slice with the plane containing the sphere centers in the phantom was facilitated with a mechanical alignment device. The device was attached to the top of the phantom (above the scanning window), and the transducer clamped onto it. Also, each phantom has a straight, permanent, waterproof mark on the scanning window which lies exactly in the plane that includes the centers of the spherical lesions. The alignment device allows linear translations of the transducer, one parallel to the mark on the scanning window and the other perpendicular to that mark and parallel to the window. The device also allows rotation of the transducer about two perpendicular axes. One (imaginary) axis is centered on the transducer face and is presumably parallel to and centered in the plane of symmetry of the scan slice. The other axis is centered on the transducer face and is also perpendicular to it. Spring-loaded screws control the alignment process. The steps in the alignment process are: 1. position the face of the transducer so that it is in contact with the scanning window, and the (imaginary) central line on the transducer face (which presumably lies in the plane of symmetry of the scan slice) contacts the mark on the scanning window; 2. rotate the transducer around the central line on the transducer face until the number of imaged spheres is maximized; 3. “fine-tune” the position and orientation of the transducer with the translation and



a)



b)

Fig. 2. (a) An image of a spherical lesion phantom with simulated lesions in a regular array. (b) An image of the spherical lesion phantom with the scan slice offset from the plane of spheres, providing an image of solely background material.

rotation screws until optimal maximization in number of imaged spheres is realized.<sup>2</sup>

Acquisition of the US image data for detection analysis includes at least one image with the scan plane superimposed over the plane of spheres (referred to as a target image) and four images of the phantom background material only, referred to as background images. (To achieve a statistically sufficient number of sphere realizations per depth interval, it may be necessary to include more than one target image.) Image data can be digitized *via* a frame-grabber board or acquired in digital format directly from the scanner. For this work, US

<sup>2</sup>Spherical lesion phantoms have been made with crossed fibers and smooth spherical reflectors to position the scan slice independently of sphere images. Experience has shown, however, that using the method described above is much more sensitive.

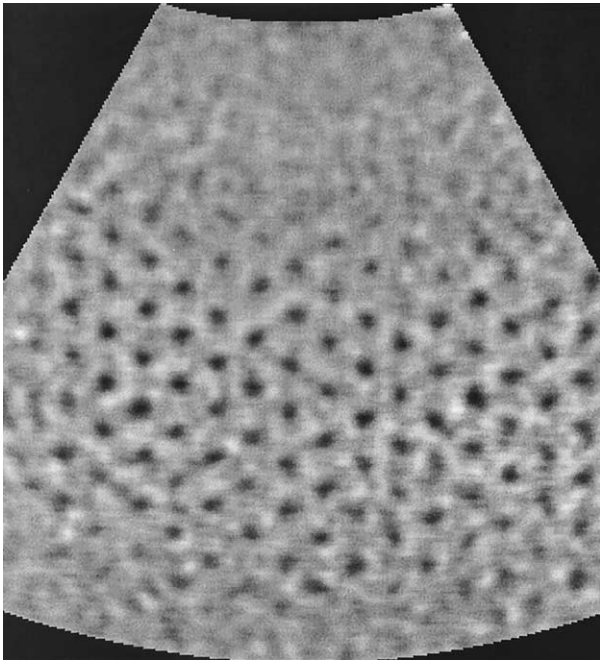


Fig. 3. An “image” of *LSNR* values that have been scaled to the 8-bit minus 1 range (0 to 254). The pixel value of 255 is reserved for masking areas surrounding the diagnostic component for nonrectangular image formats.

images were acquired on three scanner models (128XP and Sequoia models, Acuson Corp., Mountain View, CA. and model Logic 700, GE, Milwaukee, WI) and transferred in digital format to a Macintosh computer (model 9500, Apple Computer, Cupertino, CA). Scan parameters were set to provide a clinically acceptable image. Time-gain compensation was adjusted so that the displayed image was uniform in brightness throughout the imaging depth range.

#### Locating sphere positions in target images

Before *LSNR* values can be computed for the target spheres, the positions of spheres in each target image must be determined. The relative positions of spheres in the target image should correspond to those in the phantom. With that assumption, a straightforward procedure for locating the sphere positions is to determine that position of the array of points in the image such that the average of the *LSNR* values at those points is the extremum. The four steps below detail the procedure. Note that, if there are obvious image distance inaccuracies (*e.g.*, the apparent distance between spheres is 1.6 cm instead of the actual 1.5 cm), then corrective steps must be taken; such steps are described in the section “Linear distortions resulting in distance inaccuracies in the phantom images.”

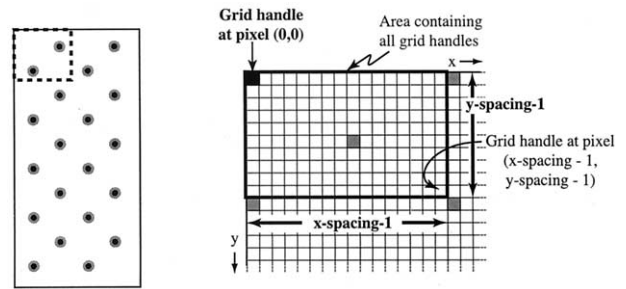


Fig. 4. The sphere array template, or virtual grid, is referenced by the topmost sphere in the first column of spheres, which is called the grid handle.

The first step is to create the virtual *LSNR* image. Software first performs the *LSNR* calculation centered at every available pixel<sup>3</sup> within the diagnostic component whether a sphere is present or not. (The diagnostic component is defined as the region of the image file that contains only echo data.) The resulting computational array of *LSNR*<sub>*Lx,y*</sub> values is scaled to a range of 0 to 254 and comprises a virtual image of *LSNR*<sub>*Lx,y*</sub> values (Fig. 3). (The value 255, which is displayed as black, is reserved for use as a mask for nonrectangular image formats.)

The second step is to calculate the average *LSNR* for virtual grids with handles at a fixed orientation. A virtual grid is a 2-D array of points with the same relative positions as the sphere centers in the phantom (see Fig. 1). The pixel location of the uppermost grid point on the left-hand side is referred to as the “grid handle” (Fig. 4). Grid handles for every possible unique virtual grid are confined to a rectangle bounded by the pixel coordinates (0, 0) and (x-spacing - 1, y-spacing - 1).

The maximum area with grid handles corresponding to unique virtual grids equals  $x_s \times y_s/2$ , where  $x_s = 1.5$  cm is the horizontal grid spacing and  $y_s = 1.0$  cm is the vertical grid spacing (see Fig. 5). To represent this maximum area, we have chosen the rectangle with dimensions  $x_s$  and  $y_s/2$  in the upper left corner of the virtual *LSNR* image depicted in Fig. 5.

Computation of the mean *LSNR* values for each grid handle is performed as follows. Define:

$$S(x_0, y_0) \equiv \sum_{n=0}^{N-1} p(x_0, y_0 + ny_s) \quad (5)$$

and

<sup>3</sup>A square region of dimension equal to the spatially calibrated lesion diameter is used for the signal component of the *LSNR* value. To reduce the number of computations,  $\sigma_B$  [see eqn (3)] is computed only over a square lattice of points with 1-mm spacing (instead of at every pixel coordinate) on background images.

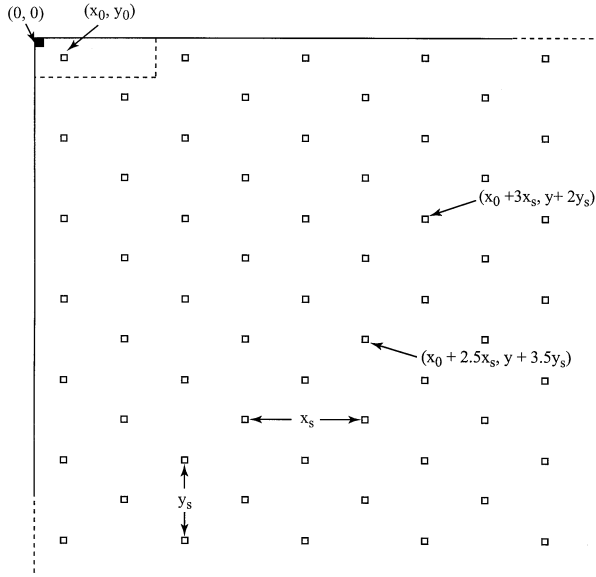


Fig. 5. Upper left region of the virtual image of  $LSNR$  values showing a virtual grid with grid handle at  $(x_0, y_0)$ . The  $y$ -axis is directed downward and the  $x$ -axis is directed from left to right. The dashed rectangle shows the region over which grid handles are sufficient for determining the optimal mean  $LSNR$  for a given grid orientation.

$$T_{\pm}(x_0, y_0) \equiv \sum_{n'=0}^{N'-1} p(x_0 \pm \frac{1}{2}x_s, y_0 + (n' + \frac{1}{2})y_s), \quad (6)$$

where  $p(x, y)$  is the  $LSNR$  pixel value with coordinates  $(x, y)$ .  $y_s = 1.0$  cm is the  $y$  spacing of the grid.  $N$  is the smallest positive integer for which  $(x_0, y_0 + Ny_s)$  lies outside the area where  $LSNR$  values are defined, and  $N'$  is the smallest positive integer for which  $(x_0 + 1/2x_s, y_0 + (N' + 1/2)y_s)$  lies outside the area where  $LSNR$  values are defined. The  $+$  sign in  $T_{\pm}$  applies when  $x_0 < x_s/2$ , and the  $-$  sign applies when  $x_s/2 \leq x_0 < x_s$ .  $x_0$  takes on values  $0, \Delta x, 2\Delta x, 3\Delta x, \dots, x_s - 1$ , and  $y_0$  takes on values  $0, \Delta y, 2\Delta y, 3\Delta y, \dots, (1/2)y_s - 1$ , where  $\Delta x$  and  $\Delta y$  are the single pixel dimensions, the pixel area being  $\Delta x \Delta y$ . The mean pixel value for the grid with grid-handle coordinates  $(x_0, y_0)$  is then:

$$\overline{LSNR}(x_0, y_0) = \frac{1}{MN + M'N'} \cdot \left[ \sum_{m=0}^{M-1} S(x_0 + mx_s, y_0) + \sum_{m'=0}^{M'-1} T(x_0 + mx_s, y_0) \right], \quad (7)$$

where  $M$  is the smallest positive integer, so that  $(x_0 + Mx_s, y_0)$  lies outside the area where  $LSNR$  values are defined, and  $M'$  is the smallest positive integer, so that

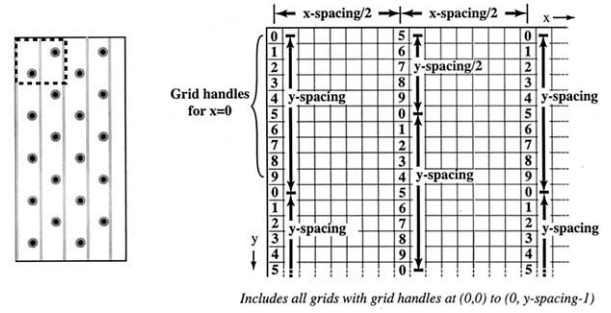


Fig. 6. Index assignment for each pixel and for each column of data in the virtual  $LSNR$  image that is associated with a grid handle at  $x = 0$ . Pixels with identical indices are members of the same virtual grid. The small number of pixels that separate the spheres in this diagram is for convenience of illustration.

$(x_0 + M'x_s, y_0)$  lies outside the area where  $LSNR$  values are defined.

Implementation of eqn (7) is achieved computationally by assigning indices to each pixel location on the virtual  $LSNR$  image, one column at a time (Madsen and Kofler 1998). Indices are first assigned to all pixel locations in the first column ( $x = 0$ ) so that each index corresponds to a unique virtual grid (Fig. 6). Therefore, the number of indices is equal to the number of pixels between adjacent sphere centers in the  $y$  direction. Indices are then assigned to pixels in the  $x = x_s/2$  column so that there is a correspondence with the virtual grid points from the column at  $x = 0$ . That is, the indices account for the staggered positioning of the matrix of spheres. Indices are assigned to the remaining columns of pixels associated with grid handles at  $x = 0$  in a similar manner; each unique index represents a virtual grid.  $LSNR$  values associated with each index are summed and the result is divided by the number of occurrences of each, which yields  $\overline{LSNR}(0, y_0)$ . The sequence is repeated for grid handles with  $x = 1$  to  $x = x_s/2 - 1$ , thereby providing average  $LSNR$  values for all possible grid locations.

To accommodate nonrectangular formatted images, a masking area between the (nonrectangular) diagnostic component and a minimal bounding rectangle is introduced; at the grid positions in the masking area, the pixel value is set to 255. During processing, pixel values of 255 do not contribute to the average  $LSNR$  value. Such a masking area is depicted in Fig. 3.

The third step is to determine average  $LSNR$  values for different orientations of the virtual  $LSNR$  image. After the average  $LSNR$  for a given set of grid handles has been determined, the virtual  $LSNR$  image is rotated by  $1^\circ$  around the geometric center of the image, and the entire process is repeated (Fig. 7). The software repeats the process for  $-5^\circ$  to  $5^\circ$  in  $1^\circ$  increments. To maintain

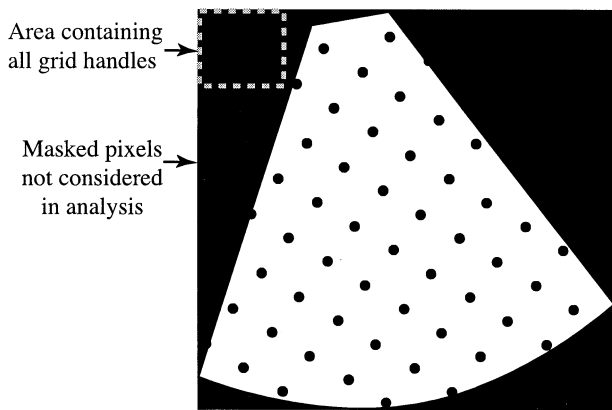


Fig. 7. The virtual  $LSNR$  image is rotated from  $-5^\circ$  to  $5^\circ$  in  $1^\circ$  increments. At each position, the grid handle of the maximum average  $LSNR$  grid is determined.

the integrity of the  $LSNR$  image for a given rotation angle, a bilinear interpolation method is used.

The fourth step is to determine the locations of the spheres. The coordinates of the grid handle and angle associated with the maximum (for positive contrast spheres) or minimum (for negative contrast spheres) grid-average  $LSNR$  determine the positions of all spheres in the image. The spacing and relative positions of the spheres within the phantom can be translated into pixel coordinates using the spatial calibration (pixels/mm) of the image.

#### *Linear distortions (distance inaccuracies) in the phantom images*

In some cases, the vertical or horizontal distance calibration accuracy of the scanner is poor, and exact superposition of the virtual grid over the array of spheres is impossible over the entire target image. To account for lateral spatial registration inaccuracies, which are more prevalent than vertical, the software repeats the entire search translation and angulation multiple times; each time the  $x$ -spacing (lateral) of the spheres is incremented by one pixel. The nominal  $x$ -spacing is varied over a range of  $-5$  to  $5$  pixels. With or without altering the expected spacing, the maximum or minimum grid-average  $LSNR$  determines the locations of the spheres.

#### *Resolution zone determination*

After the sphere positions in the image have been determined, calculation of a final set of  $LSNR$  values at each sphere location can proceed. Generally, computation of these final  $LSNR$  values involves excluding some or all of the known target lesion area for computing the mean background signal,  $S_B$  [see eqn (3)]; thus, a more

accurate value of  $S_B$  can be obtained. Such exclusion is not possible until the positions of the lesions in the image are known.

$LSNR$  values at the known positions of lesions in the image are used to determine the resolution zone for the particular diameter and object contrast of the lesions. The proximal and distal depths of the resolution zone are determined by application of a threshold  $LSNR$  value. (Such a threshold value has been determined for the lesion phantoms using an objective two-alternative forced-choice method described in a companion article.)

Random fluctuations in brightness, referred to as speckle, relate to the local arrangement of scatterers in the imaged medium. A result is that the  $LSNR$  value computed about a specific point in the image depends on the local arrangement of scatterers. Thus,  $LSNR$  values at a given depth will vary accordingly. The value used in determining detectability at a given depth is the mean,  $LSNR_M$ , of a sufficiently large number of  $LSNR$  values.  $LSNR_M$  is defined in eqn (4).

To obtain a reasonable number of  $LSNR$  values for averaging, corresponding to a given image depth,  $d$ , all values at lesion positions in the depth range ( $d - 0.5$  cm through  $d + 0.5$  cm) were employed; consideration of such a (nonzero) depth range is particularly important for scan heads other than the linear type (*e.g.*, for sector scan heads).

To determine the resolution zone, mean  $LSNR$  values over the full range of relevant image depths,  $LSNR_{M(d)}$ , are computed and a threshold value on  $LSNR_{M(d)}$  is used to determine the proximal and distal depths of the resolution zone. Values of  $d$  included might range from 0 through the image depth in, for example, 1 mm steps.

#### *Adequacy of $LSNR_M$ values*

The ideal value of  $LSNR_M$ , identified as  $LSNR_{MI}$ , results when an unlimited number of independent  $LSNR$  values at depth  $d$  contribute to the mean. Thus, any realizable number  $N$  of independent  $LSNR$  values results in an  $LSNR_{MN}$  that only approximates  $LSNR_{MI}$ . The uncertainty with which  $LSNR_{MN}$  represents  $LSNR_{MI}$  is taken to be the standard error (SD of the mean) of the  $N$  values of  $LSNR$  used to compute  $LSNR_{MN}$ .

To estimate the minimum value of  $N$  to give sufficient precision for estimating  $LSNR_{MI}$ , the following experiment was done using a linear-array 6-MHz scan head (Model 6L3, Acuson Corp., Mountain View, CA). Fifteen images were digitally acquired using a phantom containing 4-mm diameter,  $-14$  dB spherical simulated lesions. Each scan slice was centered on a single (vertical) column of spheres; in each case, the scan slice was perpendicular to the plane in the phantom containing the sphere centers. Spheres were selected at a depth such that

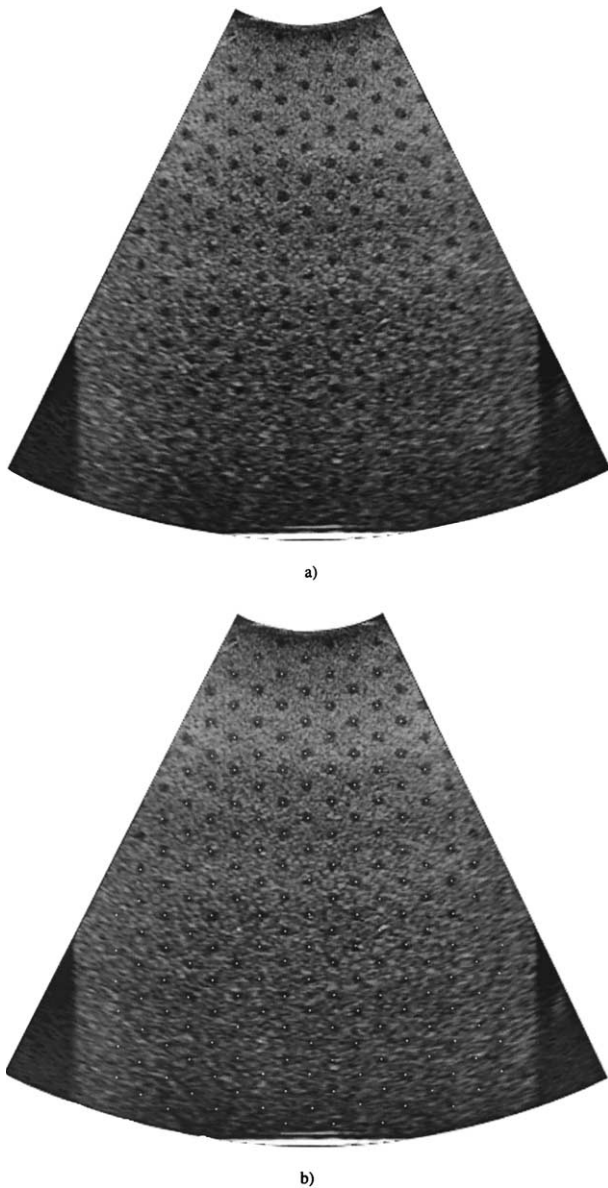


Fig. 8. (a) An image of 4-mm diameter spheres with  $-14$  dB contrast acquired with a 7-MHz sector-array transducer (maximum imaging depth 160 mm). (b) Same image as (a), with white dots showing locations of the spheres as determined *via* software.

they were borderline detectable by visual inspection of the images. Values of *LSNR* were determined for 15 different spheres for computation of the means and standard errors for  $n = 2$  through 15.

### RESULTS AND DISCUSSION

Examples showing software determination of the sphere matrix are shown in Figs. 8–10. Note that, in cases where the field-of-view (FOV) exceeds the dimen-

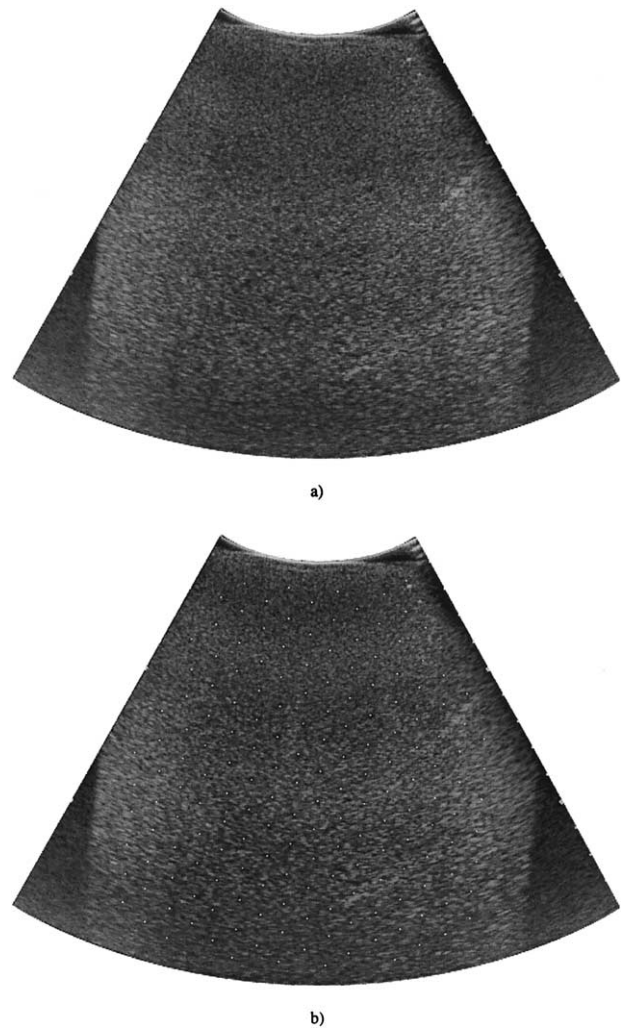


Fig. 9. (a) 3-mm diameter spheres with  $-9$  dB contrast acquired with a 5-MHz curvilinear-array transducer (maximum imaging depth 140 mm). Note that very few spheres are visible. (b) Same image as in (a), with locations of the spheres indicated by white dots as determined *via* software. In this case, the software determined that grid orientation needed to be rotated by  $5^\circ$ .

sions of the phantom, the portions of the image that do not contain phantom echo information are not included in the sphere-detection analysis. Additionally, because the *LSNR* calculation utilizes a  $1\text{ cm} \times 1\text{ cm}$  square region centered over the sphere depiction, there is a 0.5-cm border around the periphery of the image that is not valid for *LSNR* analysis. The software is able to correctly identify the sphere locations, even where those spheres are barely detectable by visual inspection, as shown in Fig. 9a and b.

Figure 10a, b and c demonstrates the ability of the lesion-locating software to account for horizontal distance error, which most commonly occurs in the case of

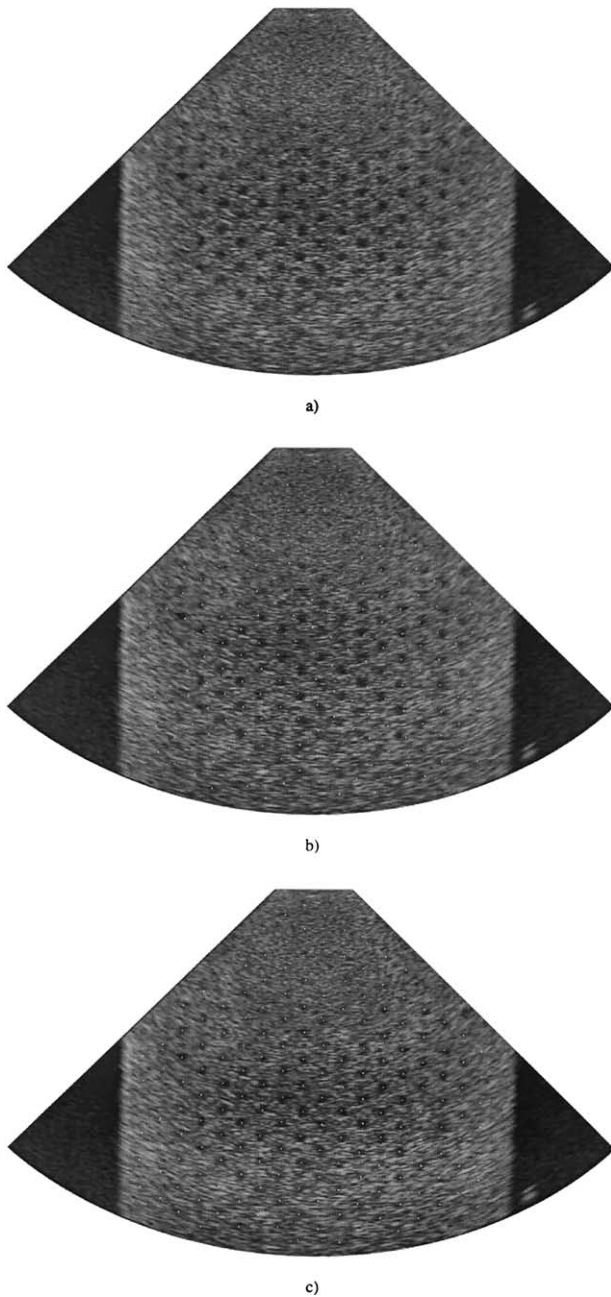


Fig. 10. (a) 5-mm diameter spheres with  $-14$  dB contrast acquired with a 4-MHz vector transducer (maximum imaging depth 140 mm). (b) Same image as in (a), with the inadequate locations of the spheres indicated by white dots, as determined *via* software. The actual sphere spacing in the phantom in the  $x$ -direction is 15 mm; however, to accurately locate the spheres, the software determined that the  $x$ -spacing of the spheres in the image is 16.8 mm. (c) Same image as in (a), with adequately determined locations of the spheres (white dots) as determined by the software with correcting for spatial miscalibration of the scanner.

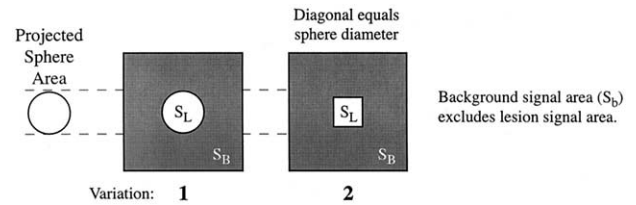


Fig. 11. The two variations of the  $LSNR$  calculation.

sector scanners. Figure 10a shows the image before the lesion-locating software has been applied. (That is, there are no white dots superimposed on the image designating lesion locations.) Figure 10b shows white dots indicating lesion positions determined by application of the software as described in the section “Locating sphere positions in target images”; the horizontal lesion spacing in the image was assumed to be 1.5 cm, as in the phantom. Visual inspection of Fig. 10b should convince the reader that many lesions have been incorrectly located. Automated variation in the assumed horizontal lesion spacing with application of the lesion-locating software produced the excellent result shown in Fig. 10c). This demonstration indicates that it is important for the user of the location software to inspect at least one sphere location result for evidence of horizontal distance error; such inspection is most important for sector scanners, and the image inspected would preferably be one in which the spheres are highly detectable over a considerable area of the image. The same distortion should occur for all phantoms imaged with a given sector scanner.

Situations that would result in poor determination of the sphere positions include varying spatial distortions and gross image artefacts (particularly if only a few spheres are visible). Sphere matrices that are angled by more than  $5^\circ$  or have spatial miscalibration in the  $x$  direction greater than 5 pixels could be accommodated, but at the expense of increased processing time. Similarly, spatial miscalibration in the  $y$  direction could also be addressed.

A the study was done to estimate the minimum number of  $LSNR$  values at depth  $d$  to yield a good approximation to  $LSNR_{MI(d)}$ . Two methods in the computation of  $LSNR$  values are presented, one using a circular region of interest (ROI) with diameter equal to the lesion diameter (method 1) and the other using a square ROI with a diagonal equal to the lesion diameter (method 2). (See Fig. 11) Fifteen different lesion images for a specific scanner configuration were employed. The depth  $d$  was chosen so that the  $LSNR$  values were near the threshold for detectability as determined by a two-alternative forced-choice (TAFC) analysis (Kofler 2000). Such a range for  $LSNR$  values

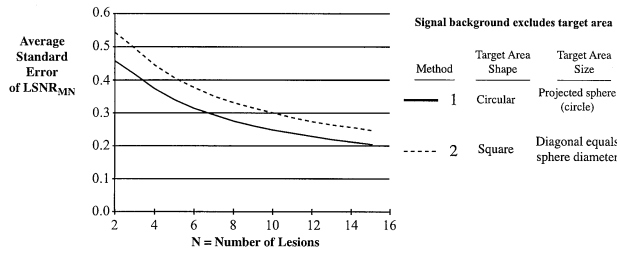


Fig. 12. The SE of the mean  $LSNR$  values vs. the number of lesions used in computing means for each  $LSNR$  calculation method. (Refer to Fig. 11 for an illustration of the methods.)

was selected because, when a threshold value is applied to determine the proximal and distal depth limits of a resolution zone, sufficiently accurate approximations to  $LSNR_{MI}$  should exist in this range. The best estimates of mean  $LSNR$  values should be  $LSNR_{M15}$  for all 15 lesions employed. For method 1,  $LSNR_{M15} = -3.06$ , and for method 2,  $LSNR_{M15} = -2.59$ .

The uncertainty with which an  $LSNR_{MN}$  value approximates the (ideal)  $LSNR_{MI}$  value was assessed for a set of  $N$  values from 2 through 15. The number of equivalent, but independent, values of  $LSNR$  available was 15. (The 15  $LSNR$  values are independent in that each corresponds to a physically different spherical lesion.) The analysis was done using each of the two methods, described in Fig. 11, for computing  $LSNR$  values. The assessment is shown in Fig. 12 where, for each value of  $N$  and each method for computing the  $LSNR$  values, the standard error (SE), or SD of the mean,  $\sum_N/(N^{1/2})$  is shown.

The following procedure was used to increase the accuracy of estimation of the SD  $\sum_N$  for  $N$  samples. There are  $15!/[(N!(15-N)!)]$  different ways to select  $N$  samples from a set of 15.  $\sum_N$  is the average sample SD over all  $15!/[(N!(15-N)!)]$  possible selections of  $N$  values. Thus,  $\sum_N/(N^{1/2})$  is an average SE corresponding to  $LSNR_{MN}$ , and the probability is about 2/3 that  $|LSNR_{MI} - LSNR_{MN}| \leq \sum_N/(N^{1/2})$ .

As expected, the plots in Fig. 12 show an approximate  $N^{-1/2}$  dependence of  $\sum_N/(N^{1/2})$ . A minimum acceptable error must be a subjective choice involving acceptable uncertainty for the depth limits of resolution zones and a practical upper limit on the number  $N$  of  $LSNR$  samples.

Of the two methods for computing  $LSNR$  values, the one for which the target area is a circle with the same diameter as the target spheres (method 1) shows the least SE. A practical minimum acceptable value for the number  $N$  of  $LSNR$  values contributing to  $LSNR_{MN}$  might be 8. Then the SE for method 1 is 0.27, less than 9% of the absolute value of  $LSNR_{M15} = 3.06$  for method 1, shown above.

A later paper will report evaluations, using the T AFC technique, of threshold values for  $LSNR_{MI}$  for effectiveness in determining resolution zones. Minimum acceptable errors of  $LSNR_{MN}$  will be addressed more thoroughly in that work.

## SUMMARY AND CONCLUSIONS

A robust method for locating the positions of spherical lesions in target images of spherical lesion phantoms has been shown to work very well. The method assumes only that the scan slice has been superimposed on the plane containing the centers of the spheres, but that the in-plane orientation of the scan head need not be restricted. Also, horizontal distance calibration error can be accounted for. If necessary, vertical distance error could also be accounted for, but the latter is far less likely to exist than horizontal error.

The method of Rownd et al. (1997) is restricted to using  $LSNR$  values computed over the entire target image. Because exact target positions were not known,  $S_B$  in eqn (3) was computed without excluding the target area on the image, and an *ad hoc* two-threshold method was employed for assessing the depth limits of the resolution zones.

Determination of the exact locations of lesion images means that depth limits of resolution zones can be determined using only  $LSNR$  values computed at the positions of the targets in the image. Also,  $LSNR$  values can be computed using  $S_B$  values where the imaged target area can be appropriately excluded. A single detectability threshold can then be applied to  $LSNR$  values to reflect human observer assessment determined *via* ROC curve or two-alternative forced-choice analyses of target vs. background images. Threshold analysis has been done using the T AFC technique (Kofler 2000) and is the subject of a future manuscript.

Evidence also was given that about eight physically independent, but equivalent,  $LSNR$  values are needed to specify accurately the ideal mean  $LSNR$  value corresponding to a given image depth.

The method for determining resolution zone limits reported in this paper for performance evaluation of US scanners is preferred to that reported in earlier studies (Rownd et al. 1997) because the positions of lesions in the image are determined and  $LSNR$  values employed are computed at lesion sites in the image. The earlier method relied on an *ad hoc* procedure with no knowledge of lesion positions in the image. Also, the method reported in this paper is tolerant of alignment errors and distance calibration errors that might occur in practical use of the technique.

*Acknowledgement*—The research described in this manuscript was supported in part by NIH grant R42GM54377.

### REFERENCES

- Kofler JM. Quantification of diagnostic ultrasound scanner performance as perceived by human observers. Ph.D. thesis. Department of Medical Physics, University of Wisconsin-Madison, 2000:98–109.
- Lopez H, Loew MH, Goodenough DJ. Objective analysis of ultrasound images by use of a computational observer. *IEEE Trans Med Imaging* 1992;2(4):496–506.
- Madsen EL, Kofler JM. US Patent number 5,827,942. System and method for testing imaging performance of ultrasound scanners and other medical imagers. 1998. USA: Wisconsin Alumni Research Foundation.
- Madsen EL, Zagzebski JA, Macdonald MC, Frank GR. Ultrasound focal lesion detectability phantoms. *Med Phys* 1991;18(6):1171–1180.
- Rownd JJ, Madsen EL, Zagzebski JA, Frank GR, Dong F. Phantoms and automated system for testing the resolution of ultrasound scanners. *Ultrasound Med Biol* 1997;23(2):245–260.
- Wagner RF, Brown DG. Unified SNR analysis of medical imaging systems. *Phys Med Biol* 1985;30(6):489–518.